Free-energy transduction mechanisms shape the flux space of metabolic networks

Benjamin Pfeuty

Free-energy transduction mechanisms shape the flux space of metabolic networks

Benjamin Pfeuty[1]

[1]Univ. Lille, CNRS, UMR 8523 - PhLAM - Physique des Lasers Atomes et Molécules, F-59000 Lille, France
[*]Corresponding author: benjamin.pfeuty@univ-lille.fr

November 18, 2024

Abstract

The transduction of free energy in metabolic networks represents a thermodynamic mechanism by which the free energy derived from nutrients is converted to drive non-spontaneous, energy-requiring metabolic reactions. This transduction is typically observed in processes that generate energy-rich molecules such as ATP and NAD(P)H, which, in turn, power specific reactions particularly biosynthetic reactions. This property establishes a pivotal connection between the intricate topology of metabolic network and their ability to reroute energy for functional purposes. The present study proposes a dedicated framework aimed at exploring the relationship between free-energy dissipation, network topology, and metabolic objectives. The starting point is that, regardless of the network topology, nonequilibrium chemostatting conditions impose stringent thermodynamic constraints on the feasible flux steady states to satisfy energy and entropy balance. An analysis of randomly-sampled reaction networks shows that the network topology imposes additional constraints that restrict the accessible flux solution space, depending on key structural features such as reaction's molecularity, reaction cycles and conservation laws. Notably, topologies featuring multimolecular reactions that implement free-energy transduction mechanisms tend to extend the accessible flux domains, facilitating the achievement of metabolic objectives such as anabolic flux maximization or flux rerouting capacity. This approach is applied to a coarse-grained model of carbohydrate metabolism, highlighting the structural requirement for optimal biomass yield.

Introduction

Cellular metabolism is a nonequilibrium process in which the free energy derived from the environment is converted into chemical work that sustains many cellular processes [Hill, 1983, Qian, 2007]. The nature and availability of free energy sources therefore impose fundamental energetic constraints that require efficient partitioning and allocation of such limited resources [Yang et al., 2021]. The landscape of free-energy dissipation throughout the metabolic network tends to be inhomogeneous and context-dependent [De Martino et al., 2012, Park et al., 2016, 2019, Niebel et al., 2019]. On the one hand, metabolic reactions operating far from equilibrium enable an efficient enzyme usage with a high chemical motive force per enzyme and flexible flux control via enzyme regulation [Park et al., 2016, Dai and Locasale, 2018]. On the other hand, reactions operating near equilibrium enable a flexible flux control by substrate and product concentrations, for instance along the glycolytic pathway [Park et al., 2019, Britt et al., 2022]. Free energies of reaction are therefore expected to subtly contribute to objective tradeoffs involving metabolic and enzyme efficiencies and determining metabolic fluxes in various conditions [Fendt et al., 2010, Schuetz et al., 2012, Maarleveld et al., 2015, Wortel et al., 2018]. Network topology itself plays an important role in determining free energies over reactions, particularly through the key roles of energy and electron/proton carriers [Reich and Selkov, 1981, Xiao et al., 2018, Rigoulet et al., 2020, Zerfaß et al., 2019, West et al., 2023] in coupling favorable and unfavorable reactions such as those in catabolic and anabolic pathways. The intricate interplay between network topology, flux objectives, and thermodynamic constraints in metabolic pathways necessitates dedicated modeling frameworks.

From a purely thermodynamic perspective, metabolic networks can be described as open chemical reaction networks (CRN) where reactions are reversible and driven by chemical motive forces [Alberty, 2005, Beard and Qian, 2007] and where nutrient sources and solvents can be considered as chemostat reservoirs, imposing nonequilibrium boundary conditions [Polettini and Esposito, 2014]. Chemical reaction network theory has been developed to explore the link between the nonequilibrium properties of flux and concentration states and the structural properties of reaction pathways [Polettini and Esposito, 2014, Rao and Esposito, 2016]. Some general relations can be established based on the breakage of conservation laws through chemostatting, or the decomposition of steady-state entropy production in terms of reaction cycles [Polettini and Esposito, 2014]. This framework is thus valuable for specifically addressing both the mechanisms and the roles

of free-energy transduction in metabolic networks. This issue can be approached at the level of specific reaction pathways [Qian and Beard, 2006, Wachtel et al., 2022] as well as through a more systematic sampling approach of chemical reaction networks. The solution spaces of dynamic models are often sampled by varying enzyme kinetic parameters, assuming implicitly regulation of enzyme activities [Schellenberger and Palsson, 2009, Machado et al., 2012, Pfeuty et al., 2023], but the topologies of metabolic reaction networks can also be sampled to capture the qualitative differences between distinct classes of topologies [Fischer et al., 2015].

The present study aims to unveil the relationships between the topology, nonequilibrium thermodynamics, and functional objectives in metabolic networks. The methods section first outlines the general framework of chemostatted chemical reaction networks, describing nonequilibrium flux states in terms of the free energy dissipation rate across reactions, and highlighting the importance of reaction cycles and conservation laws. These core thermodynamic and topological properties motivate a comprehensive approach to computing the feasible flux space, constrained primarily by chemostatting boundary conditions and subsequently by network topology. Random and systematic sampling of both kinetic and topological properties of CRNs is employed to comprehensively characterize the metabolic state space under various chemostatting conditions, addressing the significance of several topological features. First, a systematic comparison of the flux solution domains in chemical reaction networks composed of unimolecular versus bimolecular reactions highlights qualitative differences in the accessible repertoire of nonequilibrium flux states and the fulfillment of metabolic objectives related to anabolic or adaptive functions. Secondly, the minimal topologies of bimolecular CRNs that reach these metabolic objectives are identified, emphasizing the key role of free-energy transduction mechanisms and other topological requirements. Finally, the relationship between free-energy transduction mechanisms, metabolic solution space, and biomass yield objective is investigated in coarse-grained and thermodynamics-informed models of carbohydrate metabolism.

Methods

Nonequilibrium steady states in open chemical reaction networks

We consider an open chemical reaction network (CRN) comprising n_s internal species, and n_c chemostatted external species (also termed chemostat

species) whose concentrations are fixed, following a framework developed by Esposito and colleagues [Polettini and Esposito, 2014, Rao and Esposito, 2016] (Fig. 1A). The species interact through n_r reversible chemical reactions, including a set of exchange reactions with the chemostat reservoirs. The topology of the CRN is represented by the stoichiometric matrix $\mathbb{S}$, which contains the stoichiometric coefficient for the molecular species i involved in the reactions j. This matrix can be decomposed in various ways to analyze different aspects of network's structure:

$$\mathbb{S} \equiv \begin{pmatrix} \mathbb{S}^x \\ \mathbb{S}^y \end{pmatrix} \equiv \mathbb{S}^- - \mathbb{S}^+ \,, \tag{1}$$

where $\mathbb{S}^{x,y}$ contains, respectively, the stoichiometric coefficients for internal versus chemostat species, with concentrations denoted by $\vec{x}$ and $\vec{y}$, while $\mathbb{S}^{+,-}$ contains, respectively, the non-negative coefficients for forward versus backward reactions. Similarly, the net flux of a reversible reaction can be decomposed into directed forward and backward fluxes, $J_r = J_r^+ - J_r^-$, whose ratio is determined by the local detailed balance, $J_r^+/J_r^- = \exp\left(-\Delta G_r/RT\right)$ [Beard and Qian, 2007]. The chemical potential per mole of internal and chemostat species is given by $\mu_i = \mu_i^\circ + RT \ln\left(x_i/Z\right)$ and $\mu_i^y = \mu_i^{\circ,y} + RT \ln\left(y_i/Z\right)$ where R denotes the gas constant ($RT \approx 2.5\,\mathrm{kJ/mol}$ at $T = 300\,\mathrm{K}$) and Z the standard state concentration set to 1 M. The Gibbs free energy of reaction r is given by $\Delta G_r^{(\circ)} = \vec{\mu}^{(\circ)} \cdot \mathbb{S}_{:,r}$. The directed fluxes following the mass-action law are given by $J_r^{+/-} = k_r^{+/-} \prod_i x_i^{\mathbb{S}_{i,r}^{+/-}}$. Using a single overall rate constant $k_r = k_r^+ e^{\Delta G_r^\circ/2RT} = k_r^- e^{-\Delta G_r^\circ/2RT}$, the net flux can be expressed as a combination of thermodynamic and kinetic parameters:

$$J_r = k_r \left(\prod_i x_i^{\mathbb{S}_{i,r}^+} e^{-\Delta G_r^\circ/2RT} - \prod_i x_i^{\mathbb{S}_{i,r}^-} e^{\Delta G_r^\circ/2RT} \right) . \tag{2}$$

Accordingly, the steady-state flux pattern $\vec{J}$ and chemical potential pattern $\vec{\mu}$ of a CRN satisfies:

$$\mathbb{S}^x \, \vec{J}(\vec{\mu}) = 0 \,. \tag{3}$$

The nonequilibrium nature of the steady-state solution of Eq. 3 is enforced by the chemostatting condition where both the extracellular environment and the intracellular solvent can be treated as chemostat reservoirs [Polettini and Esposito, 2014]. Specifically, it is assumed that n_c internal species are exchanged with reservoirs using Fick's law of diffusion of exchanged fluxes:

$$J_r = \tilde{k}_r \left(e^{\mu_r^y/RT} - e^{\mu_r/RT} \right) \quad \text{for} \quad r = 1, ., n_c \,, \tag{4}$$

where $\tilde{k}_r = k_r\, Z\, e^{-\mu_r^\circ/RT}$ and $\mu_{r=1,.,n_c}$ denotes the chemical potential of exchanged internal species. To maintain fixed the concentrations of chemostat species, chemostat fluxes must satisfy $\vec{J}^y = -\mathbb{S}^y \vec{J}$ and are thus equal to exchange fluxes $J_r^y = J_r$ for $r = 1, ., n_c$. An important macroscopic observable of the steady state is the overall dissipation rate of free energy, that is the sum of dissipation rate for all reactions, and can be thus decomposed into the contributions of exchange versus internal reactions:

$$T\sigma = \overbrace{-\sum_{r=1}^{n_c} J_r \Delta G_r}^{T\sigma^E} \overbrace{- \sum_{r=n_c+1}^{n_r} J_r \Delta G_r}^{T\sigma^I}, \tag{5}$$

where σ is the (molar) entropy production rate. It has been demonstrated that the steady dissipation rate of a chemostatted CRN can be conveniently expressed as a function of chemostat fluxes and potentials as $T\sigma = -\vec{\mu}^y \cdot \vec{J}^y$ [Polettini and Esposito, 2014]. By treating exchanged internal species as effectively chemostatted species, a similar expression can be used for the internal dissipation rate:

$$T\sigma^I = -\sum_{i=1,n_c} \mu_i J_i \,. \tag{6}$$

The role of chemostatting in shaping the steady-state dissipation pattern is influenced by the topological properties related to reaction cycles and conservation laws [Polettini and Esposito, 2014]. The basis vectors of the right null space (kernel) of the internal stoichiometric matrix $\mathbb{S}^x$ define a set of reaction cycles $\vec{j}$, which are similar to elementary flux vectors [Klamt et al., 2017]. Following the terminology proposed in [Polettini and Esposito, 2014], these cycles are termed emergent cycles (j^{ec}), as they emerge from chemostatting some species as they do not belong to the reaction cycles of the entire non-chemostatted CRN ($\mathbb{S}\vec{j}^{ec} \neq 0$). Reaction cycles of both the internal CRN and the entire non-chemostatted CRN are termed closed cycles ($\mathbb{S}\vec{j}^{cc} = \mathbb{S}^x\vec{j}^{cc} = 0$), as they do not involve exchange reactions with chemostats. A key functional distinction is that only emergent cycles carry a flux that dissipates chemostat free energy. The basis vectors of the left null space (cokernel) of $\mathbb{S}$ define conservation vectors denoted $\vec{\ell} = (\vec{\ell}^x, \vec{\ell}^y)$, where $\vec{\ell}^x.\vec{x} + \vec{\ell}^y.\vec{y}$ remains conserved over time. Chemostatting some species leads to broken conservation laws when $\vec{\ell}^y \neq 0$ meaning that conserved quantities, such as mass or atom nuclei, are exchanged with reservoirs, thereby imposing a linear constraint on chemostat fluxes (see Supporting Material for details):

$$\vec{\ell}^y.\vec{J}^y = 0 \tag{7}$$

Importantly, the respective numbers of boundary conservation vectors n_{bc} and emergent cycles n_{ec} are linked and bounded by the relation $n_{bc} + n_{ec} = n_c$. Another topological feature of interest is the molecularity of a reaction n_m, i.e., number of reactants involved in an elementary reaction. Two main classes of network topologies can be distinguished based on whether internal reactions are exclusively unimolecular $n_m = 1$ or bimolecular $n_m = 2$, both characterized with the same mass conservation vector $\vec{\ell} = \vec{1}$.

Feasible flux space constrained by chemostatting and network topology

A steady chemostat flux state $\vec{J}^y$ is considered thermodynamically feasible when it satisfies the weak criterion of non-negative internal entropy production $\sigma^I \geq 0$ (Fig. 1B). The values $\vec{J}^y$ that correspond to the boundary $\sigma^I = 0$ of this thermodynamically feasible flux space can be determined by combining Eqs. 4 and 6, in addition to the conservation constraint given by Eq. 7:

$$\sum_{i=1,n_c} J_i^y \log\left(e^{\mu_i^y/RT} - J_i^y/\tilde{k}_i\right) = 0 \tag{8a}$$

$$\vec{\ell}^{y,i}.\vec{J}^y = 0 \quad \text{for} \quad i = 1, n_{bc}\,. \tag{8b}$$

The boundary manifold is of dimension $n_c - n_{bc} - 1 \equiv n_{ec} - 1$ and fully determined by the chemostatting condition: the chemical potentials of chemostat species $\vec{\mu}^y$, the exchange rate constants with chemostat reservoirs $k_{r=1,n_c}$ and the chemostat part of broken conservation laws $\vec{\ell}^{y,i=1,n_{bc}}$. The largest feasible flux space is thus obtained when there is a single broken conservation vector associated with mass conservation. Adding conservation constraints associated for instance to atomic composition of chemosttated species would restrict the feasible flux space to a subspace of lowest dimensionality.

A CRN of given topological and thermodynamic structure (defined by $\mathbb{S}^x$ and $\vec{\mu}^\circ$) covers a subdomain of such feasible space, but can approach the boundary manifold in some asymptotic limit in the kinetic space, such that $\Delta G_{i=n_c+1,n_r} \to 0$ and $\sigma^I \to 0$. For such quasi-equilibrium state, species chemical potentials are a linear combination of conservation vectors [Rao and Esposito, 2016] with $\mu_{i=1,n_c} = \sum_{j=1,n_{bc}} \alpha_j \ell_i^{y,j}$ given that $\ell_i^x = \ell_i^y$. Eq. 8a can be rewritten as a function of $\mu_{i=1,n_c}$ instead of J_i^y to finally obtain:

$$\sum_{i=1,n_c} \tilde{k}_i \left(\sum_{j=1,n_{bc}} \alpha_j \ell_i^{y,j}\right) \left(e^{\mu_i^y/RT} - \prod_{j=1,n_{bc}} e^{\alpha_j \ell_i^{y,j}/RT}\right) = 0 \tag{9}$$

For a general class of chemostatted CRNs with a single broken mass conservation vector ($n_{bc} = 1$ and $\vec{\ell} = \vec{1}$), $\vec{\mu} = \mu^* \vec{1}$ is incorporated into Eq. 9 to obtain:

$$\sum_{i=1,n_c} \tilde{k}_i \left(e^{\mu_i^y/RT} - e^{\mu^*/RT} \right) = 0 \,. \tag{10}$$

The unique solution μ^* of Eq. 10 is replaced into Eq. 4 to obtain the chemostat flux solutions $\vec{J}^y$ and the overall dissipation rate given by Eq. 5:

$$T\sigma^* = \sum_{i=1,n_c} \mu_i^y \, \tilde{k}_i \left(e^{\mu_i^y/RT} - \frac{\sum_i \tilde{k}_i e^{\mu_i^y/RT}}{\sum_i \tilde{k}_i} \right) . \tag{11}$$

For $n_{bc} = 1$ and $\vec{\ell} = \vec{1}$, the only nonequilibrium steady state of vanishing internal entropy production is featured with homogeneous chemical potentials $\mu_i = \mu^*$ and maximum entropy production rate $\sigma = \sigma^*$. This state can be naively illustrated in the simplest chemostatted CRN $y_1 \leftrightarrow x_1 \leftrightarrow x_2 \leftrightarrow y_2$. In the limit $k_3 \gg k_{1,2}$, the steady-state concentrations of x_1 and x_2 are dominated by the backward and forward fluxes through r_3, resutling in quasi-equilibrium ($\Delta G_3 \to 0$ and $\mu_1 \approx \mu_2$) and maximal entropy production rate $\sigma \to \sigma^*$ (Eq. 11). In the opposite limit $k_3 \ll k_{1,2}$, the exchange reactions are in quasi-equilibrium ($\mu_1 \approx \mu_1^y$ and $\mu_2 \approx \mu_2^y$) such that $J_{1,2,3} \approx 0$ and $\sigma \to 0$. $T\sigma^I = -J_3 \Delta G_3$ therefore vanishes in these two limits and reaches a maximum between.

Sampling approach

A sampling approach is designed to investigate how the solution domain in the space of exchanged fluxes depends on the network topology (Fig. 1C). It involves computing solutions to the steady-state equation Eq. 3 while randomly sampling the rate constant parameters $\vec{k}_r$, the standard chemical potentials $\vec{\mu}^\circ$ and the stoichiometric matrices $\mathbb{S}$ associated with a given class of topology. The sampling procedure is detailed in the section 1.2 and Table S1 of the Supporting Material and summarized below. The sample size ranges between 10^4 and 10^6, which is set on a case-by-case basis to avoid both undersampling and oversampling. The sampled range of thermodynamic parameters is $\mu^\circ_{i=1,n_s} \in [-6, 6]\,\mathrm{kJ/mol}$ (unless otherwise specified). The sampled range of kinetic rate constants is $k_{r=n_c+1,n_r} \in [10^{-2}, 10]$ in units of s^{-1} or $\mathrm{s}^{-1}.\mathrm{M}^{-1}$, respectively for unimolecular or bimolecular reaction, given a normalized time unit with $k_{r=1,n_c} = 1\,\mathrm{s}^{-1}$. Random stoichiometric matrices $\mathbb{S}^x$ are generated by randomly choosing substrates and products for all reactions with certain restrictions: (i) an equal number of reactants and

products, (ii) the same species cannot be both a substrate and a product (excluding autocatalytic reactions), (iii) the exclusion of duplicated reaction schemes. Some topological hyperparameters are fixed, such as the size of the CRN set to $n_s = 8$ and $n_r = 12$ (unless otherwise specified), and the same molecularity for all internal reactions set to $n_m = 1$ or $n_m = 2$. This specific sampling approach is complemented by control simulations to ensure that the qualitative results are not sensitive to network size or sampled parameter ranges (Figs. S2-S3). The volume of the sampled solution space relative to the volume of the feasible flux space is quantified by:

$$\mathcal{V} = \frac{\int_{-\infty}^{+\infty} f_2(\vec{J}^y, \mathbb{S}, \vec{\mu}^\circ)\, dJ_1^y \cdots dJ_{n_c-1}^y}{\int_{-\infty}^{+\infty} f_1(\vec{J}^y)\, dJ_1^y \cdots dJ_{n_c-1}^y} \tag{12}$$

where $f_1(\vec{J}^y) = 1$ when the criteria of thermodynamic feasibility (Eq. 8) is met and 0 otherwise, and $f_2(\vec{J}^y, .) = 1$ when a steady-state solution of Eq. 3 can be found by sampling k values in a CRN of given topology.

Results

Nonequilibrium patterns of free-energy dissipation in random chemical reaction networks

A CRN coupled to two chemostats is the most basic framework for performing a random sampling analysis of nonequilibrium properties, such as the overall versus the internal dissipation rates (Eqs. 5 and 6; Fig. 2A). First, the overall dissipation rates across a large set of CRNs with random topologies and kinetic rates (see Methods) are broadly distributed between 0 and the maximum value σ^* computed with Eq. 11 (upper panel of Fig. 2B). Characteristics of the distribution weakly depend on the network size and reaction molecularity (middle panel of Fig. 2B), while it significantly depends on the averaged kinetic constant of internal reactions $k_{r=n_c+1,n_r}$ (lower panel of Fig. 2B). Faster (resp. slower) internal reactions are correlated with higher dissipation rates, consistent with the predicted asymptotic behaviors where $\sigma^I \to 0$ and $\sigma \to \sigma^*$ for $k_{r=n_c+1,n_r} \gg k_{r=1,n_c}$. In this limit, the internal concentration states of the CRN are dominated by internal reaction fluxes such that the system converges to a quasi-equilibrium state.

In these random CRNs, the pattern of free energy, flux and entropy production over reactions exhibits a typical dependency on the overall dissipation rate $T\sigma$ (Fig. 2C). Regardless whether reactions are unimolecular or bimolecular, the sampled states of maximum entropy production rate $\sigma \lesssim \sigma^*$

are characterized with $\Delta G \to 0$ (near-equilibrium internal reactions) and $\mu_i \to \mu^*$ given by Eq. 10 (homogeneous chemical potentials). More interestingly, an increased dissipation rate in random CRNs coincides with increased maximum reaction fluxes and decreased maximum reaction free energies or species chemical energies. Such opposing trends manifest themselves with a maximal value of internal dissipation rate $T\sigma^I$ for a non-maxium level of total dissipation rate $T\sigma$, highlighting a tradeoff where the free-energy dissipation through internal reactions necessitates the dissipation of chemostat free energy to power some internal flux but also dissipate chemostat free energy which is no longer available to power fluxes through exchanged reactions. The quantitative characteristics of such tradeoff, however, depends on the chemostatting parameters such as their chemical potentials (Fig. S4).

The main difference between unimolecular and bimolecular reaction networks lies in the strict bounding of thermodynamic quantities (compare left and right panels of Fig. 2C). In unimolecular CRNs, the chemical potentials of internals species range between the chemical potentials of the two exchanged internal species with $\mu_2^y \leq \mu_2 \leq \mu_i \leq \mu_1 \leq \mu_1^y$, imposing an upper bound on the free energies of all reactions with $|\Delta G_r| \leq \mu_1 - \mu_2 \leq \mu_1^y - \mu_2^y$. In contrast, bimolecular CRNs exhibit a much broader range of nonequilibrium thermodynamic states, often violating the aforementioned bounds. This behavior can be attributed to both the increased free energy from additional metabolites involved in the reactions and the greater degrees of freedom resulting from the multivariate dependencies of the reaction rates. Such broader steady-state solution domain in the space of chemical potentials and free energies can lead to qualitative functional differences in the high-dimensional flux state space, an issue that is explored in the following sections.

Requirement for multimolecular reactions and free-energy transduction to achieve anabolic function

To investigate more thoroughly how the accessible flux space is determined by the network topology, we consider CRNs coupled to a third chemostat reservoir with a chemical potential hierarchy $\mu_3^y > \mu_1^y > \mu_2^y$ (Fig. 3A). A negative exchange flux $J_3 < 0$ thus mimics an anabolic or biosynthetic process that produces energy-rich compounds, here assumed to be exported from the CRN. Given such chemostatting conditions, the two-dimensional feasible flux space can be computed using Eq. 8, showing that maximum entropy production $\sigma = \sigma^*$ would coincide with the maximum influx of energy-rich compounds ($J_3 > 0$), whereas maximum efflux of energy-rich

species $-J_3 = J^*$ occurs for a much lower entropy production rate (black lines and violet circles in Fig. 3B,C). The capacity of CRNs to achieve negative J_3 values is investigated by computing the steady flux solutions of Eq 3 for a large set of CRNs of randomly-varied topologies and kinetics, distinguishing two main classes of topologies: unimolecular and bimolecular reaction networks. Unimolecular reaction networks fail to achieve an anabolic flux mode with $J_3 < 0$ (Fig. 3B), which can be naively explained by the allowed range of chemical potentials $(\mu^y)^{\min} < \mu_i < (\mu^y)^{\max}$ precluding $J_3 < 0$ as μ_3 cannot be larger than the highest chemostat potential μ_3^y. Relieved from this constraint, bimolecular reaction networks cover the entire feasible flux domain, including the anabolic mode where $J_3 < 0$ and approaching the maximum feasible value $-J_3 = J^*$ (Fig. 3C).

Given that bimolecular reaction networks can virtually cover the entire feasible flux domain, the subsequent inquiry revolves around characterizing the topological features required to reach the anabolic objective of maximizing $-J_3$. The flux solution domain of diverse bimolecular CRN topologies can be kinetically sampled and shows a very distinct capacity of maximizing $-J_3$, ranging from $(-J_3)^{max}$ being positive, slightly negative, or close to J^* (Fig. 3D). The distribution of the maximum anabolic flux $(-J_3)^{max}$ across randomly-sampled CRN topologies demonstrates indeed that only a small fraction of multimolecular network topologies can display an anabolic flux, where the small subset having two broken conservation laws ($n_{bc} = 2$) is more prone to achieving the maximum anabolic flux as depicted by the shape of the sampled distribution (Fig. 3E). The key topological features required for reaching anabolic objectives can be identified by seeking the reaction network of minimal topological complexity that achieves $-J_3 \simeq J^*$. The minimal CRN with optimal anabolic capacity comprises a simple set of $n_r = 5$ reactions involving $n_s = 5$ species, including two non-exchanged internal species whose interconversions are coupled to the reactions interconverting exchanged internal species (Fig. 3F). The substantial chemical energy difference between these two non-exchanged internal species, where $\mu_4 \gg \mu_5$, drives the transduction of free energy released in the conversion from the nutrient species μ_1 into the waste species μ_2, to power the conversion from nutrient species to anabolic species μ_3. This free-energy transduction process supporting anabolic function is implemented at the level of the stoichiometric matrix through the existence of one emergent cycle, and importantly also, two broken and one unbroken conservation vectors (mass conservation: $\vec{\ell}^{x,1} = \vec{1}$; structural conservation: $\vec{\ell}^{x,2} = [2, 0, 4, 1, -1]$; energy-carrier conservation: $\vec{\ell}^{x,3} = [0, 0, 0, 1, 1]$). Accordingly, the kinetically sampled flux solution domain of this minimal model coincides with

a line along a single elementary flux vector approaching the optimal state $J_3 = J^*$ for fast enough internal reaction constants k_4 and k_5 (Fig. 3G). In relation to Eq. 9, this quasiequilibrium state is indeed decomposable into conservation laws $\vec{\mu} = \sum_{i=1,3} \alpha_i \vec{\ell}^{x,i}$ where $\vec{\alpha} \approx [-4.2, 2.84, 2.84]$. Fig. 3G also shows that this one-dimensional flux domain associated with maximum $-J_3$ is one of many flux line domains associated with CRNs containing two nontrivial conservation laws. It is remarkable that those CRNs cover only domains that are inaccessible to unimolecular networks (compare Figs. 3G and 3B). Although two broken conservation laws are neither sufficient nor necessary to exhibit states associated with $J_3 < 0$, the role of this topological feature in maximizing $-J_3$, regardless of network size, demonstrates the requirement for specific structural constraints to optimally redirect free energy for anabolic purposes.

Requirement for closed cycles and free-energy transduction to achieve metabolic flexibility

In addition to biosynthetic objectives, the ability to flexibly reroute fluxes through regulated kinetics is a crucial aspect of metabolic function. To address this issue, we consider a slightly different chemostatting protocol involving two nutrient species, with equally high chemical potential, and one waste species with much lower chemical potential (Fig. 4A). The goal is to explore whether certain topologies exhibit a greater capacity to manifest a broad range of functional flux states, such as co-consumption, selective consumption, or export of nutrient species. Similar to the previous chemostatting condition investigated in Fig. 3, only bimolecular reaction networks demonstrate the ability to fully access the whole thermodynamically feasible flux space, including flux states characterized with the export of nutrient-like species $J_{1,2} < 0$ (compare Figs. 4B and C).

The subsequent question is whether and which specific CRN topologies are more prone to display the broadest flux solution domain including states that maximize exchange fluxes. Again, the flux solution domains of diverse bimolecular CRN topologies can be kinetically sampled and show very distinct flux domain size quantified by a normalized volume $\mathcal{V}$ using Eq. 12 (Fig. 4D). Distribution of $\mathcal{V}$ across a random set of CRN topologies broadly ranges between 0 and 1, but different topologies are more or less prone to display a broad flux solution space. Unimolecular reaction networks show two peaks, around 0.6 associated with the capacity to fill the whole sampled space shown in Fig. 4B, and half this value associated with topologies prone to import preferentially one of the two nutrient species. In contrast,

bimolecular reaction networks shown a broader range of flux domain size including smaller and larger flux domains than unimolecular reaction networks. Interestingly, only bimolecular reaction networks involving closed reaction cycles are statistically much more prone to display highest values for $\mathcal{V}$ approaching one (Fig. 4E). It is worth noting that, for the same number of species, the number of closed cycles increases with the number of reactions or the number of unbroken conservation laws. The key topological features required for displaying the broadest flux solution domain can be again identified by seeking for the CRN of minimal complexity that maximizes $\mathcal{V}$. Such minimal topology is shown to comprise $n_r = 7$ reactions between $n_s = 5$ species, including one unbroken conservation law where $x_4 + x_5 = L$ and one closed cycle involving all internal reactions (Fig. 4F). Kinetic sampling of this minimal CRN highlights that steady-state flux solutions cover nearly the entire feasible space, including the possibility of reaching the boundary of the feasible flux space at several locations corresponding to the modes of co-consumption, selective consumption and selective export of each nutrient (Fig. 4G). The presence of a closed cycle confers the possibility to implement various simple CRN topologies capable of achieving a given optimal flux configuration. For instance, $k_{4,5} = 0$ or $k_{6,7} = 0$ would generate minimal network topologies similar to the one depicted in Fig. 3F: each of these topologies is characterized by two broken conservation laws and the ability to maximize the export flux of either nutrient species. It is also worth noting that the sampled flux states are all associated with $\mu_4 > \mu_5$, indicating that the same energy-carrier species is exploited to transduce free energy to sustain a diversity of functional flux modes.

In summary, the functional capacity to exhibit a very diverse range of flux states is enhanced in network topologies comprising closed cycles, which provide flexibility, and multimolecular reactions implementing free-energy transduction mechanisms, enabling an expanded coverage of the thermodynamically feasible flux space.

Case study of a coarse-grained model of carbohydrate metabolism

Multimolecular reactions and free-energy transduction mechanisms are common in cellular metabolic pathways, notably through reaction coupling involving energy carriers such as ATP or NAD(P)H. The aim of this section is to apply the proposed framework to a coarse-grained model of carbohydrate metabolism and investigate whether the relations between free-energy transduction mechanisms and the geometry of the metabolic solution space hold true. Consistent with the assumption of a chemostatted CRN, some

internal species are exchanged with chemostat reservoirs (i.e., glucose, acetate, water, carbon dioxide, oxygen, protons, biomass), while others are not (Acetyl-CoA, ADP and ATP). Besides ATP, other important energy carriers, such as NAD(P)H, are implicitly considered for through conversion factors, although strict conservation laws for associated moieties are not enforced. The metabolic pathways that interconvert exchanged species with internal species (glycolysis, fermentation, aerobic respiration, biomass synthesis, and basal ATP consumption) are described as single effective reactions (Fig. 5A). The set of simplifying assumptions and thermodynamic properties of this coarse-grained model are detailed in the Supporting Material and Table S2.

The assumption of steady chemostatting conditions allows for a strict application of the framework designed to depict and compare the thermodynamically feasible and kinetically sampled flux spaces (Fig. 5B). On the one hand, the chemostatting properties and the conservation laws associated with atom and other moieties (see Table S2) define the thermodynamically feasible domain in the space of exchange fluxes using Eq. 8. On the other hand, kinetic sampling of the steady-state flux solutions using Eqs 2 and 3 determines the accessible flux subdomain, highlighting whether the topology is well-suited for maximizing a given flux objective. This comparative approach can be applied to any chemostatting condition of interest, here associated with glucose and oxygen availability and lack of acetate, providing several insights into the anabolic state of highest biomass yield (Fig. 5C). Firstly, the sampled flux solution domain is polyhedron-shaped with vertices corresponding to elementary flux modes (Table S2) or their combinations, associated with a full fermentation mode, full aerobic respiration mode and maximal biomass production through either fermentation only or respiration only. Similar solution polyhedra and their vertices are obtained with a constraint-based stoichiometric modeling approach, with the additional constraint imposed by the steady solutions in the chemical potential (or concentration) space. Secondly, the sampled flux solution domain covers a broad, but not complete, part of the thermodynamically feasible flux space, revealing topological constraints on thermodynamic efficiency. Accordingly, the optimal biomass yield obtained from kinetic sampling is lower that the maximum biomass yield constrained by conservation laws and thermodynamics, and much lower than the maximum biomass yield considering carbon conservation only, where all glycolytic carbons are converted into biomass carbons (dashed lines in Fig. 5C). Lastly, the paradoxical result shown in Fig. 3 where maximum anabolic flux coincides with non-maximum nutrient import is still valid, but not observable as $J_{gex} \lesssim J_{gex}^{max}$ (left panel of Fig. 5C), due to higher chemical potential difference between chemostat

species.

An important result obtained from the thermodynamic and sampling analysis of random CRN is that free-energy transduction mechanisms, implemented by a specific topologies, are crucial for efficient anabolic functions and biomass yield. In the carbohydrate metabolism model, the sampled solution domain in the space of biomass flux versus total dissipation rates shows that a higher optimal biomass yield correlates with lower dissipation rates (i.e., $T\sigma^{opt} \ll T\sigma^{*} \approx 60\text{kJ/l/h}$) (Fig. 6A). The characteristics β^{max}, β^{opt} or $T\sigma^{opt}$ of these optimal biomass-yield states depend on model parameters (Fig. S5), such as the standard chemical potentiel of the effective biomass species, chemostatting parameters like oxygen availability, and network topological properties such as ATP demand and yield per reaction. It is noteworthy that solutions seem to approach the feasible space boundary where $\sigma^{I} = 0$, but a closer examination reveals that asymptotically reaching this quasi-equilibrium state is challenging due to the high standard free energies of many reactions (Fig. S4). The role of free energy transduction in determining β^{opt} is investigated by modulating the ATP yield of both glycolytic and respiratory reactions ($\mathbb{S}_{ATP,gly/ares}$). A higher ATP yield in both reactions results in a broader flux solution domain and an increased optimal biomass yield (Fig. 6B). This effect is mediated by changes in free-energy efficiency through ATP-producing reactions, defined as the ratio of the output over the input of free energy in a coupled process [Wachtel et al., 2022]:

$$\eta_j = -\frac{S_{ATP,j}(\mu_{ATP} + \mu_{H_2O} - \mu_{ADP'})}{\mu_{prod,j} - \mu_{subs,j}} \,. \tag{13}$$

This efficiency varies between 0 (uncoupling) and 1 (maximum efficiency at equilibrium of the coupled reaction). For a given topology, free-energy transduction efficiencies can significantly vary depending on kinetically sampled flux states, but they also increase strongly in stoichiometric matrices with higher ATP yield per reactions (Fig. 6C). A more systematic computation of optimal biomass yield β^{opt} as a function of ATP yield per reaction $\mathbb{S}_{ATP,gly/ares}$ shows that biomass yield can approach its maximum feasible value β^{max} (Fig. 6D). Interestingly, the optimal biomass yield drops after a certain level of ATP yield due to the thermodynamically unfavorable glycolytic and respiratory reactions, given constraints on ADP and ATP concentrations. In summary, the structural properties and feasible space geometry of the carbohydrate metabolic model coincide with those of the small subset of sampled random multimolecular CRNs that achieves anabolic objectives, though there are notable differences related to higher standard free

energies in the coarse-grained metabolic pathways.

Discussion

Feasibility constraints and optimality principles offer a powerful explanatory framework for the observed metabolic phenotypes with respect to high-dimensional metabolic solution space [Schuetz et al., 2012, Maarleveld et al., 2015]. Such framework suitably matches with a nonequilibrium thermodynamics characterization of metabolic phenotypes, particularly in terms of their entropy production rates, or equivalently free energy dissipation rates, at both the reaction and system levels [Unrean and Srienc, 2011, Himeoka and Kaneko, 2014, Niebel et al., 2019]. Nonequilibrium chemostatting conditions are sufficient to draw a thermodynamically feasible domain in the space of exchanged fluxes bounded by a manifold of vanishing internal entropy production. The geometry of this feasible space is shaped by concentrations, standard chemical potential and exchange rates, and conservation laws of the chemostat species. This space also displays few singular states, characterized by null or maximum total entropy production, and those associated with maximum internal entropy production. Of particular interest is a subdomain within the feasible space that is accessible only through multimolecular networks that implement free-energy transduction mechanisms. This includes flux states associated with export of energy-rich species, similar to biomass production fueled by the free energy derived from nutrients and transduced by energy carriers. Based on this analogy, the theory suggests that achieving the highest biomass yield necessitates maximizing free-energy transduction efficiencies through near-equilibrium reactions, which turns out to be challenged by experimental data. Free-energy transduction in the energy-producing pathways such as glycolysis, fermentation, TCA, and ETC is far from reaching the maximum efficiency of 1, with estimates ranging between 0.3 and 0.6 [Wachtel et al., 2022]. This aligns with the observation of significant dissipation of free energy in specific reactions such as PFK, PK, ATP synthase reactions [Canelas et al., 2011, Park et al., 2016, Niebel et al., 2019]. A plausible hypothesis for this discrepancy is that dissipative, far-from-equilibrium reactions facilitate more efficient enzyme usage and are therefore more effective targets for regulating pathway flux [Park et al., 2016, Noor et al., 2016]. It would be intriguing to address whether an optimal level for free-energy transduction efficiency could emerge from combining constraints about enzyme utilization, flux controllability, and thermodynamic efficiency. This issue intersects with the search for cellular-scale

constraints, such as those associated with overflow metabolism [De Groot et al., 2020], including limits on free energy dissipation rate [Niebel et al., 2019], constraints on protein allocation [Basan et al., 2015], or considerations of macromolecular crowding effects [Beg et al., 2007].

In constraint-based stoichiometric modeling approaches, feasible flux solution spaces generally correspond to flux polyhedra resulting from the intersection of the null space and a region defined by a set of inhomogeneous linear constraints, such as bounded flux capacity or thermodynamically unfeasible directionalities [Schellenberger et al., 2011, Klamt et al., 2017]. In particular, thermodynamics-based metabolic flux analysis integrates constraints based on experimental ranges of metabolite concentrations to restrict the solution flux space and facilitate flux analysis [Henry et al., 2007]. Although related through the concept of thermodynamically feasible extreme pathways, the present approach provides a different perspective based on network topology rather than on flux estimation or flux prediction. In this respect, two distinct types of constraints are here considered: exchange fluxes are constrained by nonequilibrium chemostatting conditions, and internal fluxes are constrained by thermodynamic forces imposed by steady-state concentrations. Distinguishing between external and internal constraints allows for the definition of chemostatting-dependent flux solution space and subsequent determination of how much this space is occupied by flux solutions of a given network topology. This approach identifies topological features that contribute to the efficient utilization of thermodynamic forces to achieve metabolic objectives such as flux maximization or flux rerouting. In other words, optimal states, coinciding in constraint-based stoichiometric modeling with the vertices of the flux polyhedron [Maarleveld et al., 2015, Klamt et al., 2017], can potentially be improved or impaired by specific modifications of the network topology, be it through regulation [Nikerel et al., 2012] or truncation [Court et al., 2015, Long et al., 2018].

A key topological feature is the multimolecularity of chemical reactions, common in metabolic networks due to the chemical interactions between molecules of heterogeneous atomic composition [Haraldsdóttir and Fleming, 2016] and between multiple reactants among them energy and electron carriers [Zerfaß et al., 2019]. The ability of multimolecular reaction networks to effectively achieve diverse metabolic objectives can be interpreted from several related features that distinguish them from unimolecular reaction networks. Firstly, multimolecular mass-action reactions introduce nonlinearities that generate a greater variability in species chemical potentials and, consequently, a broader range of nonequilibrium concentration states [Fischer et al., 2015]. Secondly, multimolecular reactions structurally im-

plement energy coupling and free-energy transduction mechanisms [Wachtel et al., 2022], not only between pathways but also more generally between elementary flux modes. Lastly, the complex stoichiometries of multimolecular networks commonly exhibit non-trivial conservation laws [Dal Cengio et al., 2023], enabling a variety of optimal flux configurations beyond those maximizing the entropy production rates. This particular property of multimolecular networks relates to their hypergraph structure, which has motivated graph-theoretical and geometrical approaches to nonequilibrium reaction networks [Dal Cengio et al., 2023].

The relevance of a nonequilibrium thermodynamic framework is particularly valuable for studying metabolic shifts associated with diverse chemostatting conditions, such as changes in nutrient sources [Wang et al., 2019, Millard et al., 2023] or the division of labor and metabolite exchanges in microbial communities [Perrin et al., 2020, Kost et al., 2023]. Nonequilibrium models do not necessarily strive for the scalability of constraint-based stoichiometric modeling approaches, given the challenges in providing a self-consistent thermodynamic description of genome-scale models. Coarse-grained or modular models [Avanzini et al., 2023, Mori et al., 2023] are better suited for including the main pathways involved in metabolic flexibility. Notably, pathway motifs such as cycles, bypasses, and shunts, are likely to increase the number of reactions relative to species and to provide flexible flux rerouting in a regulation-dependent or chemostat-dependent manner [Flamholz et al., 2013, Long et al., 2018, Schink et al., 2022]. In such models, considering various moieties (e.g., phosphate, nicotinamide, CoA) is crucial for exploring the role of conservation constraints in energy and biosynthetic metabolism. Besides investigating the design logic of cellular metabolic networks, it is also appealing to refine the theoretical framework concerning the restrictive assumptions of steady state and reversible mass-action kinetics. The analysis of stability, fluctuations, or responses to driven time-dependent chemostat conditions [Rao and Esposito, 2016] would enable understanding dynamic behaviors such as metabolic shifts [Schink et al., 2022], jamming and flux limits due to conserved moieties [Hatakeyama and Furusawa, 2017, West et al., 2023] or instabilities arising from autocatalytic cycles [Barenholz et al., 2017]. Furthermore, integrating saturated reaction kinetics, which also relies on thermodynamic considerations [Ooka et al., 2023, Sahin et al., 2023], represents a natural continuation in exploring the interplay between thermodynamic and concentration-dependent contributions in shaping the flux space of a metabolic network.

Data and materials availability

All Fortran codes and data used in this study are available at github.com/bpfeuty/CRN_fluxspace.

Author contributions

The author designed the research, carried out all simulations and wrote the manuscript.

Acknowledgments

This work has been supported by the LABEX CEMPI (ANR-11-LABX-0007).

Declaration of interests

The author declares no competing interests.

Supplementary Material

An online supplement to this article can be found by visiting BJ Online at http://www.biophysj.org.

Supporting citations

References [Famili and Palsson, 2003, Lin et al., 2020, Sughiyama et al., 2022, Battley, 1992, Flamholz et al., 2012, Milo et al., 2010] appear in the supporting material.

References

R. A. Alberty. *Thermodynamics of biochemical reactions*. John Wiley & Sons, 2005.

F. Avanzini, N. Freitas, and M. Esposito. Circuit theory for chemical reaction networks. *Phys. Rev. X*, 13(2):021041, 2023.

U. Barenholz, D. Davidi, E. Reznik, Y. Bar-On, N. Antonovsky, E. Noor, and R. Milo. Design principles of autocatalytic cycles constrain enzyme kinetics and force low substrate saturation at flux branch points. *Elife*, 6: e20667, 2017.

M. Basan, S. Hui, H. Okano, Z. Zhang, Y. Shen, J. R. Williamson, and T. Hwa. Overflow metabolism in escherichia coli results from efficient proteome allocation. *Nature*, 528(7580):99–104, 2015.

E. H. Battley. On the enthalpy of formation of escherichia coli k-12 cells. *Biotechnol. Bioeng.*, 39(1):5–12, 1992.

D. A. Beard and H. Qian. Relationship between thermodynamic driving force and one-way fluxes in reversible processes. *PloS One*, 2(1):e144, 2007.

Q. K. Beg, A. Vazquez, J. Ernst, M. A. de Menezes, Z. Bar-Joseph, A.-L. Barabási, and Z. N. Oltvai. Intracellular crowding defines the mode and sequence of substrate uptake by escherichia coli and constrains its metabolic activity. *Proc. Natl. Acad. Sci.*, 104(31):12663–12668, 2007.

E. C. Britt, J. Lika, M. A. Giese, T. J. Schoen, G. L. Seim, Z. Huang, P. Y. Lee, A. Huttenlocher, and J. Fan. Switching to the cyclic pentose phosphate pathway powers the oxidative burst in activated neutrophils. *Nat. Metab.*, 4(3):389–403, 2022.

A. B. Canelas, C. Ras, A. ten Pierick, W. M. van Gulik, and J. J. Heijnen. An in vivo data-driven framework for classification and quantification of enzyme kinetics and determination of apparent thermodynamic data. *Metab. Eng.*, 13(3):294–306, 2011.

S. J. Court, B. Waclaw, and R. J. Allen. Lower glycolysis carries a higher flux than any biochemically possible alternative. *Nat. Commun.*, 6(1): 8427, 2015.

Z. Dai and J. W. Locasale. Thermodynamic constraints on the regulation of metabolic fluxes. *J. Biol. Chem.*, 293(51):19725–19739, 2018.

S. Dal Cengio, V. Lecomte, and M. Polettini. Geometry of nonequilibrium reaction networks. *Phys. Rev. X*, 13(2):021040, 2023.

D. H. De Groot, J. Lischke, R. Muolo, R. Planqué, F. J. Bruggeman, and B. Teusink. The common message of constraint-based optimization

approaches: overflow metabolism is caused by two growth-limiting constraints. *Cell. Mol. Life Sci.*, 77:441–453, 2020.

D. De Martino, M. Figliuzzi, A. De Martino, and E. Marinari. A scalable algorithm to explore the gibbs energy landscape of genome-scale metabolic networks. *PLoS Comput. Biol.*, 8(6):e1002562, 2012.

I. Famili and B. O. Palsson. The convex basis of the left null space of the stoichiometric matrix leads to the definition of metabolically meaningful pools. *Biophys. J.*, 85(1):16–26, 2003.

S.-M. Fendt, J. M. Buescher, F. Rudroff, P. Picotti, N. Zamboni, and U. Sauer. Tradeoff between enzyme and metabolite efficiency maintains metabolic homeostasis upon perturbations in enzyme capacity. *Mol. Syst. Biol.*, 6(1):356, 2010.

J. Fischer, A. Kleidon, and P. Dittrich. Thermodynamics of random reaction networks. *PLoS One*, 10(2):e0117312, 2015.

A. Flamholz, E. Noor, A. Bar-Even, and R. Milo. equilibrator—the biochemical thermodynamics calculator. *Nucleic Acids Res.*, 40(D1):D770–D775, 2012.

A. Flamholz, E. Noor, A. Bar-Even, W. Liebermeister, and R. Milo. Glycolytic strategy as a tradeoff between energy yield and protein cost. *Proc. Natl. Acad. Sci.*, 110(24):10039–10044, 2013.

H. S. Haraldsdóttir and R. M. Fleming. Identification of conserved moieties in metabolic networks by graph theoretical analysis of atom transition networks. *PLOS Comput. Biol.*, 12(11):e1004999, 2016.

T. S. Hatakeyama and C. Furusawa. Metabolic dynamics restricted by conserved carriers: Jamming and feedback. *PLoS Comput. Biol.*, 13(11): e1005847, 2017.

C. S. Henry, L. J. Broadbelt, and V. Hatzimanikatis. Thermodynamics-based metabolic flux analysis. *Biophys. J.*, 92(5):1792–1805, 2007.

T. L. Hill. Some general principles in free energy transduction. *Proc. Natl. Acad. Sci.*, 80(10):2922–2925, 1983.

Y. Himeoka and K. Kaneko. Entropy production of a steady-growth cell with catalytic reactions. *Phys. Rev. E*, 90(4):042714, 2014.

S. Klamt, G. Regensburger, M. P. Gerstl, C. Jungreuthmayer, S. Schuster, R. Mahadevan, J. Zanghellini, and S. Müller. From elementary flux modes to elementary flux vectors: Metabolic pathway analysis with arbitrary linear flux constraints. *PLoS Comput. Biol.*, 13(4):e1005409, 2017.

C. Kost, K. R. Patil, J. Friedman, S. L. Garcia, and M. Ralser. Metabolic exchanges are ubiquitous in natural microbial communities. *"Nat. Microbiol."*, 8(12):2244–2252, 2023.

W.-H. Lin, E. Kussell, L.-S. Young, and C. Jacobs-Wagner. Origin of exponential growth in nonlinear reaction networks. *Proc. Natl. Acad. Sci.*, 117(45):27795–27804, 2020.

C. P. Long, J. E. Gonzalez, A. M. Feist, B. O. Palsson, and M. R. Antoniewicz. Dissecting the genetic and metabolic mechanisms of adaptation to the knockout of a major metabolic enzyme in escherichia coli. *Proc. Natl. Acad. Sci.*, 115(1):222–227, 2018.

T. R. Maarleveld, M. T. Wortel, B. G. Olivier, B. Teusink, and F. J. Bruggeman. Interplay between constraints, objectives, and optimality for genome-scale stoichiometric models. *PLoS Comput. Biol.*, 11(4):e1004166, 2015.

D. Machado, R. S. Costa, E. C. Ferreira, I. Rocha, and B. Tidor. Exploring the gap between dynamic and constraint-based models of metabolism. *Metab. Eng.*, 14(2):112–119, 2012.

P. Millard, T. Gosselin-Monplaisir, S. Uttenweiler-Joseph, and B. Enjalbert. Acetate is a beneficial nutrient for e. coli at low glycolytic flux. *EMBO J.*, page e113079, 2023.

R. Milo, P. Jorgensen, U. Moran, G. Weber, and M. Springer. Bionumbers—the database of key numbers in molecular and cell biology. *Nucleic Acids Res.*, 38(suppl_1):D750–D753, 2010.

M. Mori, C. Cheng, B. R. Taylor, H. Okano, and T. Hwa. Functional decomposition of metabolism allows a system-level quantification of fluxes and protein allocation towards specific metabolic functions. *Nat. Commun.*, 14(1):4161, 2023.

B. Niebel, S. Leupold, and M. Heinemann. An upper limit on gibbs energy dissipation governs cellular metabolism. *Nat. Metab.*, 1(1):125–132, 2019.

E. Nikerel, J. Berkhout, F. Hu, B. Teusink, M. J. Reinders, and D. De Ridder. Understanding regulation of metabolism through feasibility analysis. *PLoS One*, 7(7):e39396, 2012.

E. Noor, A. Flamholz, A. Bar-Even, D. Davidi, R. Milo, and W. Liebermeister. The protein cost of metabolic fluxes: prediction from enzymatic rate laws and cost minimization. *PLoS Comput. Biol.*, 12(11):e1005167, 2016.

H. Ooka, Y. Chiba, and R. Nakamura. Thermodynamic principle to enhance enzymatic activity using the substrate affinity. *Nat. Commun.*, 14(1):4860, 2023.

J. O. Park, S. A. Rubin, Y.-F. Xu, D. Amador-Noguez, J. Fan, T. Shlomi, and J. D. Rabinowitz. Metabolite concentrations, fluxes and free energies imply efficient enzyme usage. *Nat. Chem. Biol.*, 12(7):482–489, 2016.

J. O. Park, L. B. Tanner, M. H. Wei, D. B. Khana, T. B. Jacobson, Z. Zhang, S. A. Rubin, S. H.-J. Li, M. B. Higgins, D. M. Stevenson, et al. Near-equilibrium glycolysis supports metabolic homeostasis and energy yield. *Nat. Chem. Biol.*, 15(10):1001–1008, 2019.

E. Perrin, V. Ghini, M. Giovannini, F. Di Patti, B. Cardazzo, L. Carraro, C. Fagorzi, P. Turano, R. Fani, and M. Fondi. Diauxie and co-utilization of carbon sources can coexist during bacterial growth in nutritionally complex environments. *Nat. Commun.*, 11(1):3135, 2020.

B. Pfeuty, J. Hurbain, and Q. Thommen. Control analysis of cooperativity and complementarity in metabolic regulations: The case of nadph homeostasis. *Metabolites*, 13(4):485, 2023.

M. Polettini and M. Esposito. Irreversible thermodynamics of open chemical networks. i. emergent cycles and broken conservation laws. *J. Chem. Phys.*, 141(2):07B610_1, 2014.

H. Qian. Phosphorylation energy hypothesis: open chemical systems and their biological functions. *Annu. Rev. Phys. Chem.*, 58:113–142, 2007.

H. Qian and D. A. Beard. Metabolic futile cycles and their functions: a systems analysis of energy and control. *IEE Proceedings-Systems Biol.*, 153(4):192–200, 2006.

R. Rao and M. Esposito. Nonequilibrium thermodynamics of chemical reaction networks: wisdom from stochastic thermodynamics. *Phys. Rev. X*, 6(4):041064, 2016.

J. G. Reich and E. E. Selkov. *Energy metabolism of the cell*. New York: Academic, 1981.

M. Rigoulet, C. Bouchez, P. Paumard, S. Ransac, S. Cuvellier, S. Duvezin-Caubet, J. Mazat, and A. Devin. Cell energy metabolism: An update. *Biochim. Et Biophys. Acta -Bioenergetics*, 1861(11):148276, 2020.

A. Sahin, D. R. Weilandt, and V. Hatzimanikatis. Optimal enzyme utilization suggests that concentrations and thermodynamics determine binding mechanisms and enzyme saturations. *Nat. Commun.*, 14(1):2618, 2023.

J. Schellenberger and B. Ø. Palsson. Use of randomized sampling for analysis of metabolic networks. *J. Biol. Chem.*, 284(9):5457–5461, 2009.

J. Schellenberger, N. E. Lewis, and B. Ø. Palsson. Elimination of thermodynamically infeasible loops in steady-state metabolic models. *Biophys. J.*, 100(3):544–553, 2011.

S. J. Schink, D. Christodoulou, A. Mukherjee, E. Athaide, V. Brunner, T. Fuhrer, G. A. Bradshaw, U. Sauer, and M. Basan. Glycolysis/gluconeogenesis specialization in microbes is driven by biochemical constraints of flux sensing. *Mol. Syst. Biol.*, 18(1):e10704, 2022.

R. Schuetz, N. Zamboni, M. Zampieri, M. Heinemann, and U. Sauer. Multidimensional optimality of microbial metabolism. *Science*, 336(6081): 601–604, 2012.

Y. Sughiyama, A. Kamimura, D. Loutchko, and T. J. Kobayashi. Chemical thermodynamics for growing systems. *Phys. Rev. Res.*, 4(3):033191, 2022.

P. Unrean and F. Srienc. Metabolic networks evolve towards states of maximum entropy production. *Metab. Eng.*, 13(6):666–673, 2011.

A. Wachtel, R. Rao, and M. Esposito. Free-energy transduction in chemical reaction networks: From enzymes to metabolism. *J. Chem. Phys.*, 157 (2):024109, 2022.

X. Wang, K. Xia, X. Yang, and C. Tang. Growth strategy of microbes on mixed carbon sources. *Nat. Commun.*, 10(1):1279, 2019.

R. West, H. Delattre, E. Noor, E. Feliu, and O. S. Soyer. Dynamics of co-substrate pools can constrain and regulate metabolic fluxes. *Elife*, 12: e84379, 2023.

M. T. Wortel, E. Noor, M. Ferris, F. J. Bruggeman, and W. Liebermeister. Metabolic enzyme cost explains variable trade-offs between microbial growth rate and yield. *PLoS Comput. Biol.*, 14(2):e1006010, 2018.

W. Xiao, R.-S. Wang, D. E. Handy, and J. Loscalzo. Nad (h) and nadp (h) redox couples and cellular energy metabolism. *Antioxid. & Redox Signal.*, 28(3):251–272, 2018.

X. Yang, M. Heinemann, J. Howard, G. Huber, S. Iyer-Biswas, G. Le Treut, M. Lynch, K. L. Montooth, D. J. Needleman, S. Pigolotti, et al. Physical bioenergetics: Energy fluxes, budgets, and constraints in cells. *Proc. Natl. Acad. Sci.*, 118(26):e2026786118, 2021.

C. Zerfaß, M. Asally, and O. S. Soyer. Interrogating metabolism as an electron flow system. *Curr. Opin. In Syst. Biol.*, 13:59–67, 2019.

Figure legends

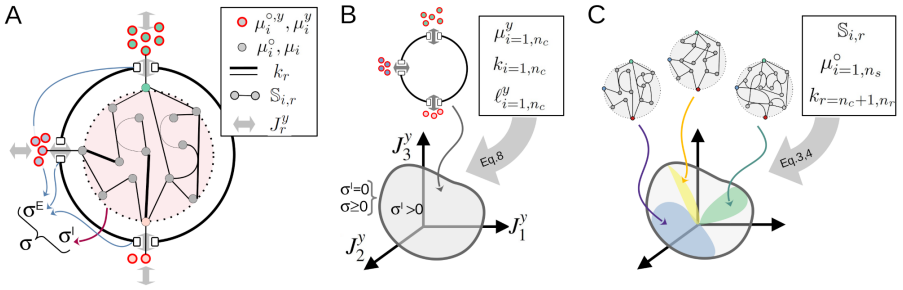

Figure 1: **Feasible and restricted flux spaces in chemostatted chemical reaction networks.** (A) Schematic representation of an open chemostatted chemical reaction network involving n_c chemostat species (bold red-outlined circle) and n_s internal species (circles) of standard chemical potential μ°. The network includes internal and exchanged reactions (lines) with kinetic rate constants k_r, and is described by a stoichiometric matrix $\mathbb{S}$. Steady-state variables of interest include the species' chemical potentials μ_i, chemostat fluxes J^y and total entropy production rate σ or, equivalently, chemostat free-energy dissipation rate $T\sigma$, which can be decomposed into contributions from exchanged and internal reactions: $\sigma = \sigma^E + \sigma^I$. (B) The chemostatting conditions ($\vec{\mu}^y$, $k_{r=1,n_c}$) and the conservation laws ($\vec{\ell}$) define a thermodynamically feasible flux solution domain in the space of exchange fluxes bounded by a manifold where $\sigma^I = 0$ (Eq. 8). (C) The stoichiometric matrices of diverse network topologies exhibit different kinetically sampled chemostat flux solution domain (Eq. 3).

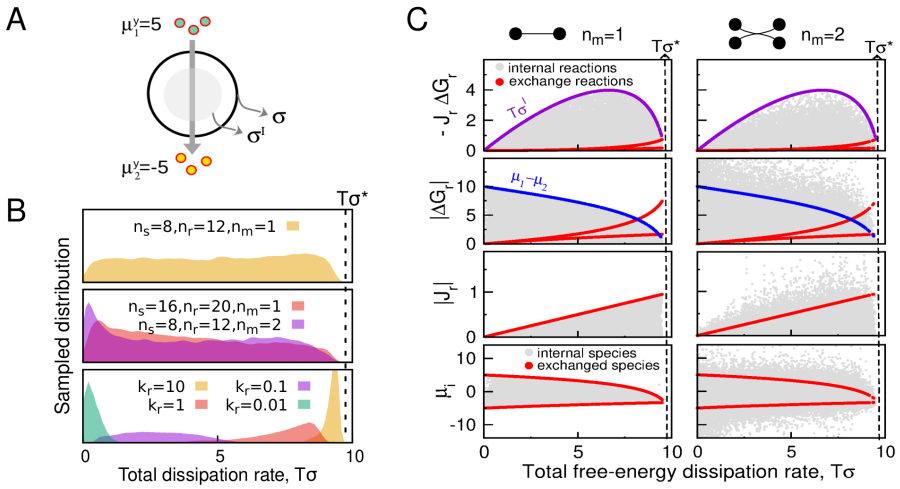

Figure 2: **Distribution and bounds of thermodynamic variables in random CRNs**. (A) CRN coupled to two chemostats ($\vec{\mu}^y = [5, -5]$, $\vec{y} = \vec{1}$ and $k_{1,2} = 1$) characterized by a maximum dissipation rate of $T\sigma^* \approx 9.64$ computed using Eq. 11. (B) Probability distribution functions of $T\sigma$ (Eq. 5) for a set of 10^5 random CRNs with random $\mathbb{S}^x$, $k_{r=n_c+1,n_r}$ and μ_i°. Upper panel: default values for n_s, n_r and n_m. Middle panel: Example of varied values for n_m or n_s and n_r. Lower panel: same as upper panel, but with fixed kinetic rate constants $k_{r=n_c+1,n_r} = 0.01$, 0.1, 1, or 10 instead of randomly sampled. (C) Distribution of thermodynamic variables associated with reactions and species as a function of the total free-energy dissipation rate $T\sigma$ in the CRN, for a set of 10^4 random CRNs with unimolecular (left panels) or bimolecular (right panels) reactions. The violet line represents $T\sigma^I$ computed from Eq. 7, and the blue line represents $\mu_1 - \mu_2$, bounding the reaction free energy only for $n_m = 1$. All quantities are expressed in units listed in Table S1.

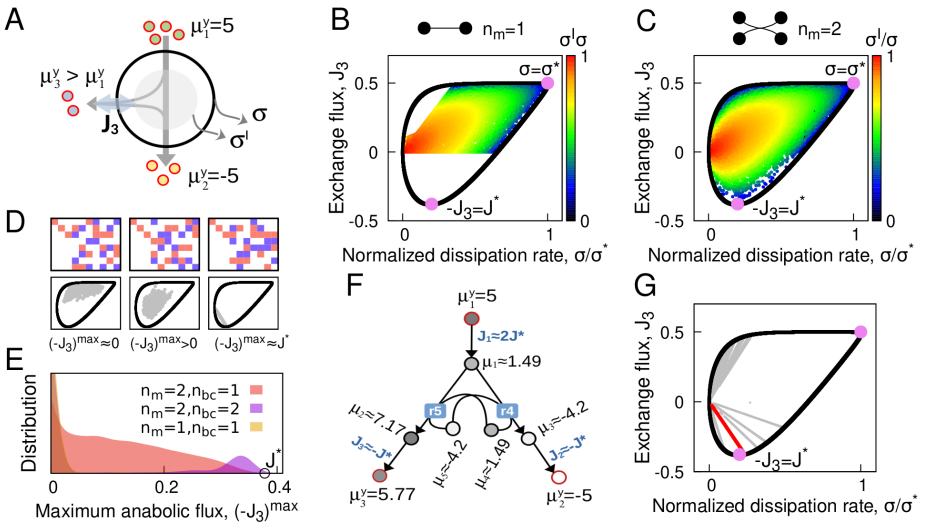

Figure 3: **Anabolic capacity in bimolecular reaction networks.** (A) CRN coupled to three chemostats ($\vec{\mu}^y = [5, -5, 5.77]$, $\vec{y} = [1, 1, 0.5]$ and $k_{1,..,n_c} = 1$), focusing on the maximization of an anabolic-like flux $-J_3$. (B) Thermodynamically feasible solution domains (black line computed by solving Eq. 8) and sampled solutions of 10^4 random unimolecular CRNs (dots where color denotes the internal contribution to entropy production σ^I/σ) plotted in the space the exchange flux J_3 and the normalized entropy production rate σ/σ^*. (C) Similar to (B), but for 5×10^4 random bimolecular CRNs ($n_m = 2$). (D) Examples of three CRN topologies of specific stoichiometric matrix $\mathbb{S}^x$ (red=+1; blue:−1; white:0) and their corresponding kinetically sampled solution domains (gray dots in lower panels). These topologies differ qualitatively in their maximum $(-J_3)^{max}$ values. (E) Probability distribution of $(-J_3)^{max}$ for a set of $2\,10^3$ random network topologies (each sampled with 10^3 random kinetic parameters). Topologies are sampled based on a defined topological class characterized by the number broken conservation law n_{bc} and the reaction molecularity n_m. (F) CRN of minimal topological complexity ($n_s = 5$, $n_r = 5$, $n_{bc} = 2$) characterized by a maximum anabolic exchange flux $-J_3 \simeq J^*$ (for $k_{4,5} = 10^2$). (G) Flux solution domain of the minimal CRN sampled with 10^3 random kinetic parameters (red), with respect to flux solution domain of 10^5 random CRNs with $n_{bc} = 2$ and non-zero fluxes (grey). All quantities are expressed in units listed in Table S1.

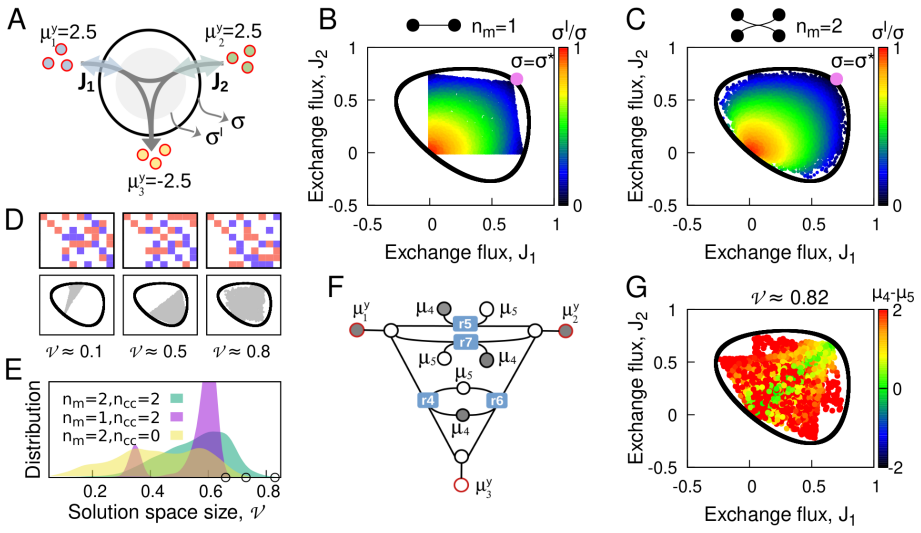

Figure 4: **Metabolic flexibility in bimolecular reaction networks.** (A) CRN coupled to three chemostats ($\vec{\mu}^y = [2.5, 2.5, -2.5]$, $\vec{y} = \vec{1}$ and $k_{1,.,n_c} = 1$), focusing on the flexible utilization of two nutrient sources. (B,C) Thermodynamically feasible flux domain (black line computed using Eq. 8) and sampled solutions of 10^4 random unimolecular reaction networks (dots, with color denoting the internal contribution to entropy production σ^I/σ), plotted in the space of exchange fluxes J_1 and J_2. (C) Similar to (B), but for 5×10^4 random bimolecular reaction networks ($n_m = 2$). (D) Examples of three CRN topologies with specific stoichiometric matrices $\mathbb{S}^x$ (red=+1; blue:−1; white:0) and their corresponding kinetically sampled solution domains (gray dots in lower panels). These topologies differ qualitatively in their flux domain size $\mathcal{V}$ (gray area normalized to the bounded area). (E) Probability density of $\mathcal{V}$ for a set of 2×10^3 random topologies (each sampled with 10^3 random kinetic parameters). Topologies are sampled based on a defined topological class characterized by the number of closed cycles n_{cc} and the reaction molecularity n_m. (F) CRN of minimal topological complexity ($n_s = 5$, $n_r = 7$, $n_{ec} = 2$, $n_{uc} = 1$, $n_{bc} = 1$, $n_{cc} = 1$) characterized with maximum domain size $\mathcal{V} \approx 0.82$. (G) Flux solution domain of the minimal CRN, with color codes representing the energy charge $\mu_4 - \mu_5$ as an indication of free-energy transduction. All quantities are expressed in units listed in Table S1.

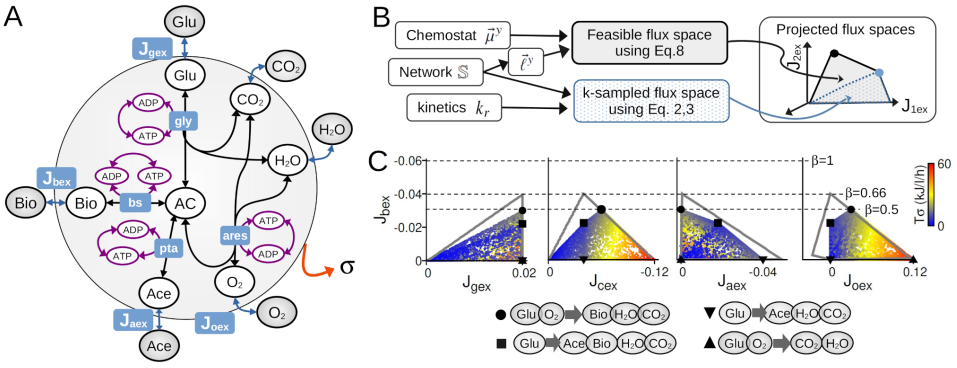

Figure 5: **Framework applied to a coarse-grained carbohydrate metabolic model.** (A) A coarse-grained metabolic network model involving $n_c = 7$ chemostat species, $n_s = 10$ internal species and $n_r = 12$ reactions (the H^+ species is not shown for readability). (B) Workflow to compare feasible and sampled spaces for a chemostatted metabolic network model. (C) Feasible solution domains and (grey lines computed by solving Eq.8) and kinetically sampled solutions of 2×10^4 reaction networks, plotted in the 2D spaces of biomass exchange flux as a function of other exchange fluxes. The sampled flux solution polyhedron displays vertices (black geometrical shapes) representing elementary flux modes. Maximum carbon-based biomass yield $\beta = -J_{bex}/J_{glu}$ is represented for the sampled solution space ($\beta \approx 0.5$), for the feasible space ($\beta \approx 0.66$) and for the case where all glycolytic carbons are converted into biomass carbons ($\beta = 1$). Chemostatting parameters are $y_{Glu} = 0.02$M, $y_{Bio} = y_{CO_2} = y_{Ace} = 0.001$M and $y_{O_2} = y_{H_2O} = y_{H^+} = 1$M, and thermodynamic and structural parameters are given in Table S2.

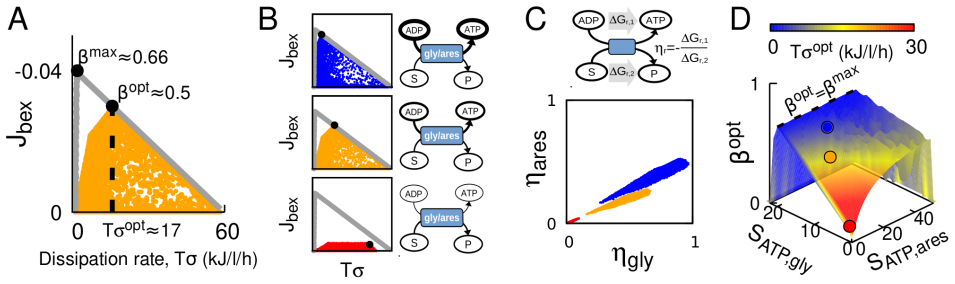

Figure 6: **Relation between biomass yield and free-energy transduction.** (A) J_{bex} as a function of the total dissipation rate, highlighting that maximum feasible $\beta = \beta^{max}$ and optimal sampled $\beta = beta^{opt}$ occurs for low dissipation rates. (B) Effect of ATP yield of glycolytic and aerobic respiratory reactions on the sampled flux solution space (bottom/red: $\mathbb{S}_{ATP,gly} = \mathbb{S}_{ATP,ares} = 1$; center/orange: $S_{ATP,gly} = S_{ATP,ares} = 10$; top/blue: $\mathbb{S}_{ATP,gly} = 15$, $S_{ATP,ares} = 20$). Circles represent the states of optimal biomass yield β^{opt} for each case. (C) Representation of the sampled solutions in (B) as a function of free-energy transduction efficiencies in glycolytic and respiratory reactions. (D) Effect of $S_{ATP,gly}$ and $S_{ATP,ares}$ on the optimal biomass yield β^{opt}. Circles represent parameters used in panels B. Dashed line represents the limit case where $\beta^{opt} = \beta^{max}$. Chemostatting parameters are $y_{Glu} = 0.02$M, $y_{Bio} = y_{CO_2} = y_{Ace} = 0.001$M and $y_{O_2} = y_{H_2O} = y_{H^+} = 1$M, and thermodynamic and structural parameters are given in Table S2.